SAND2018-5258C

Spatially Resolved Analysis of Material Response to Destructive Environments Utilizing Three-Dimensional Scans

Jeffrey D. Engerer* and Alexander L. Brown†
Sandia National Laboratories, Albuquerque, NM, 87185-1135

The surface topology of a solid subjected to destructive environments is often difficult to quantify. In thermal environments, the size and shape of the solid changes as it pyrolyzes, ablates, warps, or chars. Quantitative descriptions of such responses are valuable for data reporting and model validation. In this work, a three-dimensional scanner is evaluated for non-destructive material analysis. The scans spatially resolve the response of materials to a high-heat-flux environment. To account for the effect of distortion induced in thin materials, back-side scans of the sample are used to characterize the displacement of the bulk material. Data spanning the area of the sample, rather than using a net or average quantity, enhances the evaluation of the crater formed by the incident flux. The 3D reconstruction of the sample also provides the ability to perform volumetric calculations. The data obtained from this methodology may be useful for characterizing materials exposed to a variety of destructive environments.

I. Introduction

Post-mortem analysis of materials exposed to energetic thermal or mechanical environments often provides valuable data for a wide range of engineering applications. Material properties and physical phenomena can be identified by either qualitative or quantitative analysis of a damaged region. In the field of metallurgy, a common example is the surface morphology of ductile and brittle fracture planes [1]. In thermal environments, pyrolysis, combustion, and ablation of materials are often examined by both qualitative (e.g., charring, pitting, cracking) and quantitative (e.g., mass loss, char depth, surface recession) metrics [2, 3].

Many of these surface measurements are either localized or spatially averaged. For example, line measurements are common both in tribology, such as by surface profilometer [4], and thermal sciences, such as cross-sections on materials after pyrolysis or ablation [2, 3]. Mass loss is another common metric that does not provide spatial resolution. Full three-dimensional reconstruction of a damaged surface provides greater detail of the surface topology.

Commercial three-dimensional scanners, marketed predominantly for medical and design applications, have made this technology widely available. In mechanical environments, three-dimensional scans of fractured surfaces can reveal various physical phenomena, such as microstructural features affecting shear strength [5]. For materials damaged in thermal environments, the use of the technology is not widespread.

The objective of the current work is twofold. First, the utility of three-dimensional (3D) scanning technology is examined for materials exposed to destructive environments. A process was developed that enhanced the data obtained by the scanner. A validation experiment was performed to evaluate the accuracy of the instrument. Second, experimental data are presented for the response of materials to intense irradiation ($\sim$100 kW m^{-2}–1000 kW m^{-2}). The technique provided additional data not easily obtained by traditional methods.

II. Methods

A. The Solar Furnace

Experiments were performed at the Solar Furnace at the National Solar Thermal Test Facility (Sandia National Laboratories, Albuquerque, New Mexico). The Solar Furnace concentrates sunlight to generate intense thermal environments reaching 6000 kW m^{-2} on a spot with a roughly Gaussian spatial profile with a full-width-half-max of 4.3 cm. A heliostat uses flat mirrors with a total reflective surface area of 55 m^2 to reflect the sunlight through an attenuator (to control the amount of power) onto a large, reflective parabolic dish. The parabolic dish concentrates the

*R&D S&E Mechanical Engineering, Fire Science and Technology, MS-1135.
†R&D S&E Mechanical Engineering, Fire Science and Technology, MS-1135.

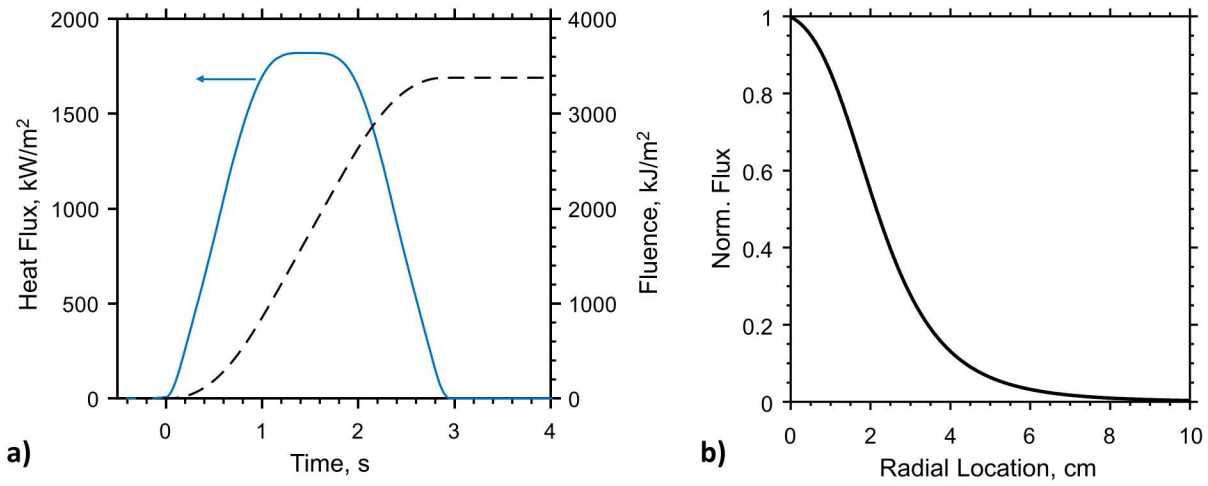

Fig. 1 Temporal and spatial profiles of the heat flux generated by the Solar Furnace. (a) Flux and the corresponding fluence produced from a nominal 4000 kJ m^{-2} exposure. (b) Radial distribution of the flux produced by the Solar Furnace. Heat flux is normalized by the value at the center of the spot.

sunlight with 228 individually aligned mirrors and has an overall diameter of 6.8 m with a focal length of 4.1 m. The mirrors are composed of silvered, low-iron glass; consequently, the spectral composition is similar to solar spectrum with attenuation in the UV and beyond 1 μm wavelength.

The irradiation during each experiment varied dynamically with the actuation (~1 s) of the attenuator. The time-varying heat flux was evaluated in separate measurements taken immediately before and after the experiment. A Kendall radiometer determined the peak heat flux reached during the experiment. A Gardon-style heat-flux gauge characterized the transient heating profile by correlating heat flux to attenuator position.

Figure 1a examines the heat flux (irradiance) and fluence produced by the Solar Furnace. The ramp in flux resulting from the actuation of the attenuator is predominantly linear. Using the transient flux data, the fluence data during the test can likewise be temporally resolved. In general, the actual exposure fluence was lower than the nominal value, predominantly due to variation in weather conditions (normal incident solar radiation).

Two main factors were identified as affecting the accuracy of the heat-flux data for these tests. First, the Kendall radiometer had an accuracy of ±2%. Second, the radiometer and heat-flux-gauge data were not recorded during the exposure of the sample; consequently, the heat flux incident on the sample was not perfectly known due to random variations in system performance and solar irradiance. Accounting for these sources of error, the accuracy of the reported flux and fluence values is ±4.3% (90% confidence).

The reported flux and fluence were measured at the center of the solar beam where irradiation was the most intense; however, the Solar Furnace did not produce a spatially uniform flux with a well-defined spot diameter. The radial distribution of irradiation is examined in Fig. 1b. The spatial variation was quantified in a previous study [6]. The spatially and temporally dependent flux is expressed in the following form:

$$q''(t,r) = \frac{q''_o(t)}{1 + \exp\left(C\left(\frac{R_0}{R_1}r\right)^D - B\right)} \tag{1}$$

where $q''_o(t)$ is the peak flux at the center of the spot, R_0 is the projected beam radius at the focal plane, R_1 is the projected beam radius outside of the focal plane, and B, C, and D are coefficients determined by the slope error of the parabolic dish. The spatial distribution produced by the solar furnace was best characterized using a slope error of 3 milliradians ($B = 6.662$, $C = 27.7$, $D = 0.401$) and assuming the ratio of the projected beam radii is $R_0/R_1 = 1.34$ [6]. This equation neglects the slight asymmetries in the real spatial profile.

B. 3D Scanner

3D scans were obtained using a NextEngine 3D Scanner Ultra HD. The device uses 650 nm lasers to scan the sample and captures data with two 5.0 Megapixel CMOS image sensors. The advertised accuracy of the scanner is 0.13 mm (0.005 in). In the majority of advertised applications, objects have significant three-dimensional features. Using the rotating sample mount, the manufacturer recommends obtaining scans at multiple angles to improve three-dimensional reconstruction, particularly when data are required on multiple surfaces.

During preliminary measurements, the three-dimensional reconstruction of thin plates (11.4 cm by 22.9 cm by 0.5 cm) using the manufacturer software and 360° scans was not successful. The software had difficulty merging scans from the front and back surfaces. This issue seems to relate to the high aspect ratio of the sample and the sharp edges. Under these circumstances, the scanner does not have sufficient data on the relative orientation of the front and back surface; consequently, small angular displacement of the front and back surface results in significant, erroneous thickness variations.

As discussed in Section III.B, some samples required three-dimensional reconstruction to obtain meaningful data; consequently, a technique was developed for scanning thin, planar samples. Alignment marks were drawn on the front and back surfaces of the samples. Front- and back-surface scans were then generated within the scanner software independently. In post-processing, the scans from the two surfaces were oriented in the transverse direction using the alignment marks. A significant angular misalignment still existed between the scans, causing the calculated thickness of sample to vary along the width and height. The angular misalignment was corrected by rotating the backside scan along the two axes parallel to the surface; the requisite rotational angles were determined by correcting the mean thickness of the material in unaffected regions.

The color of the sample surface (surface absorptivity at 650 nm) had a significant impact on the measurement. The surface topology recorded by the scanner erroneously varied with the surface absorptivity (e.g., charring from the exposure). Specular (glossy) surfaces could not be resolved. To counteract these effects, the manufacturer recommends coating surfaces with a diffuse (matte) white paint or powder. Magnaflux Spotcheck SKD-S2 Solvent-Based Developer was used for this purpose.

Surface topology, on both front- and back-surfaces, was reconstructed using three separate scans. One scan was taken normal to the surface; two were taken after rotating the sample 36 degrees in either direction. This series of scans was aligned and merged using the manufacturer software (ScanStudio HD). The data were exported as an array of spatial coordinates. These data were imported into Matlab. If necessary, the back-side scan was used to correct the distortion of the front surface, revealing features unique to the front surface (e.g., the crater produced by the exposure). The reconstructed surfaces were visualized using Delaunay triangulation. The total material (volume) loss was determined by summing the local, discrete quantity for each data point; localized volume loss was calculated from the local crater depth and the area of the respective Vornoi polygon.

III. Results

A. Scanner Validation

A validation scan was performed on a flat surface with four steps of known thickness. The validation sample was fabricated by adhering bars onto the surface of a flat plate. The thicknesses of the various features were confirmed with a micrometer (0.01 mm resolution). The three-dimensional surface reconstruction of the validation sample is provided in Fig. 2.

The validation sample revealed three forms of errors, all on the order of 0.1 mm. First, the surface profile had a significant level of noise overlaid on the data. Second, the measurement varied spatially, in a manner inconsistent with the true character of the flat sample. Third, the heights of known features were overestimated. The first two error sources are examined by scaling the color bar to the erroneous height variations in the base plane, as in Fig. 3. The noise is spatially correlated, manifested by apparent vertical striations. This noise is not due to surface roughness; the base plane of the validation sample is very smooth relative to the scanner accuracy. The noise has an RMS of approximately 0.025 mm; the corresponding probability density function is normally distributed when measured over large areas ($\sim$100 mm^2). The noise may significantly affect features smaller than 10 mm, but can otherwise be eliminated by spatially averaging the signal.

The spatial variations are more concerning, because they may alter the surface topology in regions of interest (e.g., pyrolysis crater depth). Across all of the scans, these variations are most notable in the bottom left and right corners of the scan (roughly 4 cm^2 area). Neglecting these corners, which are ignored in all subsequent analyses, the variation of

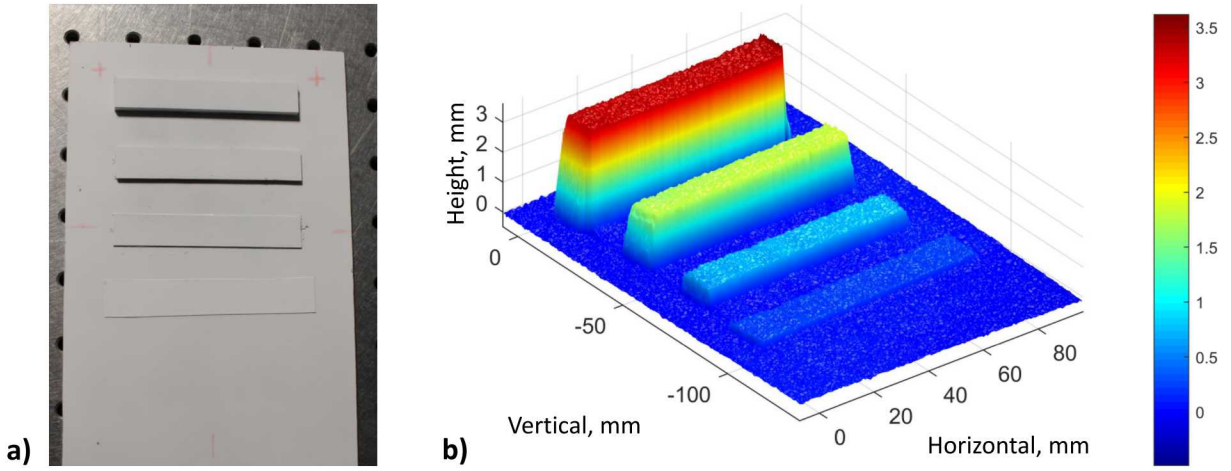

Fig. 2 Validation sample used to determine the accuracy of the 3D scanner. (a) Image of the validation sample with four steps of known height. (b) Three-dimensional reconstruction of the validation sample based on a scan of the front surface. Features in height direction have been scaled by a factor of 10 to improve visualization.

Table 1 Height of features on the validation sample. The actual height, relative to the base plane, was measured with a micrometer. The measured height and respective errors are determined from the scanner data (Fig. 2).

Step	Act. Height (mm)	Scan. Height (mm)	Meas. Error (mm)	Percent Error (%)
1	3.26	3.35	.09	3.8
2	1.66	1.73	.07	4.4
3	0.56	0.65	.09	16.0
4	0.17	0.18	.01	4.8

the surface profile is still significant. The mean sample height (after averaging over a 100 mm^2 area) varies between approximately −0.03 mm and 0.07 mm. This type of variation is difficult to characterize and varies between scans.

The third form of error, the accuracy of the surface profile, is more easily characterized using the known heights of the steps on the validation sample. Table 1 compares the data obtained from the scanner to the measurements made with the micrometer. The measured height from the 3D scan was obtained by averaging the profile height at the top of each step. The area of these steps was sufficient to eliminate the effect of measurement noise. The scanner consistently overestimated the height of the features by 0.07 mm–0.09 mm, other than for the smallest step. The calculated measurement error for the smallest step is at the resolution of the micrometer, consequently, the value is at best an order-of-magnitude estimate.

Table 1 indicates the measurement error was roughly 0.08 mm, for relatively thick features. For relatively thin features, the error was approximately 5%. Features with small area (less than ~100 mm^2) may have additional inaccuracies due to the noise exhibited in the scanner data. The advertised accuracy (0.13 mm) of the scanner is consistent with the results obtained here. Results for Step 4 indicate the instrument may accurately resolve features that are relatively thin compared to this value, but more testing would be required to verify this.

The validation scan was obtained using the same conditions and processing steps as the other samples in this study. Other variables, such as distance between the scanner and the sample, ambient lighting, and surface coatings, may impact the accuracy of the measurement. Consequently, future studies should independently confirm the accuracy of 3D scans under the conditions associated with their measurements.

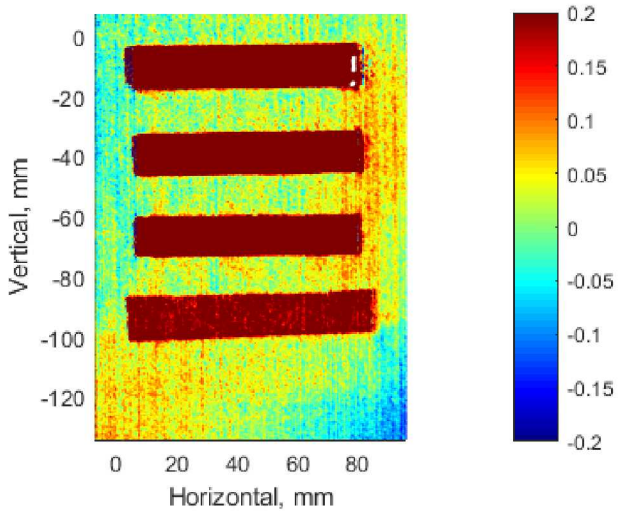

Fig. 3 Variability in the scanner measurement for the base plane of the validation sample. The surface profile (color bar) has units of millimeters.

B. Solar Furnace Samples

Although many materials were tested at the Solar Furnace, only a limited subset displayed characteristics that justified performing 3D scans. Materials selected for scanning generated a crater of significant depth (>0.1 mm), had a limited amount of deformation/melting, and did not continue to burn after the exposure. Black polymethyl-methacrylate (PMMA) and high-impact polystyrene were examined for the purposes of this study.

1. PMMA

Three PMMA samples were exposed to a fluence of roughly 3400 kJ m^{-2}. The state of the material post-exposure was favorable for scanning. The material pyrolyzed strongly, resulting in high mass loss, deep craters, and better relative measurement accuracy. The video data indicate the material rapidly decomposed and vaporized. The crater shape/depth did not appear to be significantly affected by melting of the thermoplastic. The samples were very thick (11.3 mm) and were not expected to deform; consequently, only front-surface scans were performed.

Figure 4 presents the topology of the front surface. The depth at the crater center was just under 2 mm; the crater diameter was approximately 34 mm. The apparent surface height varied spatially outside of the crater, indicating the front surface was concave due to warping of the bulk material. From the outer edge of the crater to the upper corner of the sample, the measured height varies by 0.4 mm. This moderate distortion may erroneously increase the measured crater depth.

The radial variation of crater depth and exposure fluence is provided in Fig. 5a. The crater depth is normalized by the value just outside the crater rim. The radial distributions of the crater depth and fluence are similar, especially near the center. Crater depth was approximately linearly correlated to the local exposure fluence, as displayed in Figure 5b. These data indicate the material no longer pyrolyzes when the local exposure fluence drops below roughly 800 kJ m^{-2}.

Assuming the material remaining after the exposure has the same density as the virgin material, the spatially resolved mass flux, m'', can be estimated from the local crater depth, z, using the following expression:

$$m'' = \rho * \Delta z \tag{2}$$

where ρ is the density (1.20 g cm^{-3}) of the virgin material. Applying this expression, the net mass flux at the center of the crater ($\approx$1.9 mm deep) was approximately 0.23 g cm^{-2}.

Utilizing these same assumptions, the net volume loss is used to calculate the mass loss. The mass loss was independently measured using the pre- and post-test weight of the sample. These data, and the associated errors, are provided in Table 2. Similar to the validation scan, the data indicate the scanner significantly overestimates the depth

variation (crater depth); however, the error is much larger than indicated by the validation scan. Step 2 (1.66 mm) on the validation sample had comparable height variation and was resolved by the scanner with only 4.4% error. The mass-loss error (≈12%) for the PMMA samples is significantly higher. The accuracy of the mass-loss estimation may have been significantly influenced by the distortion noted in Fig. 4.

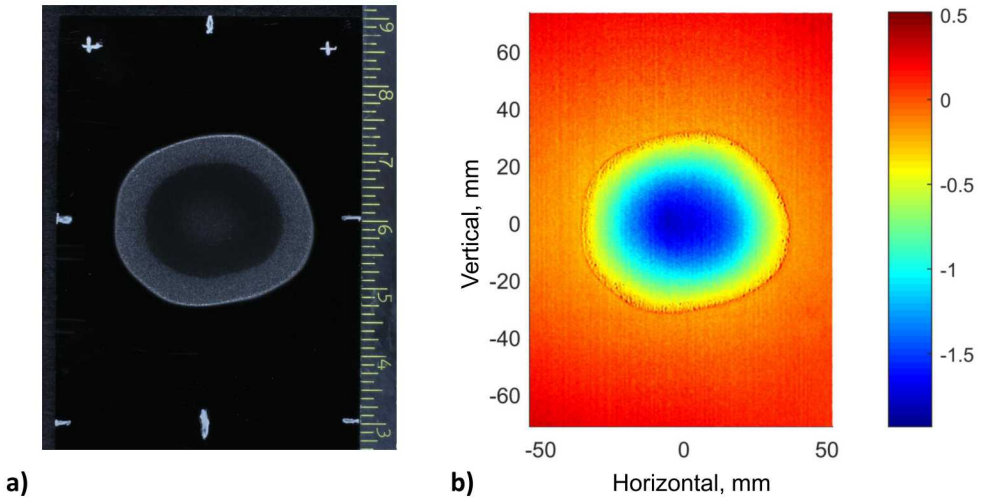

Fig. 4 Comparison of (a) PMMA-sample photograph and (b) the corresponding front-surface scan. Ruler in photograph has units of inches. The surface profile (color bar) has units of millimeters.

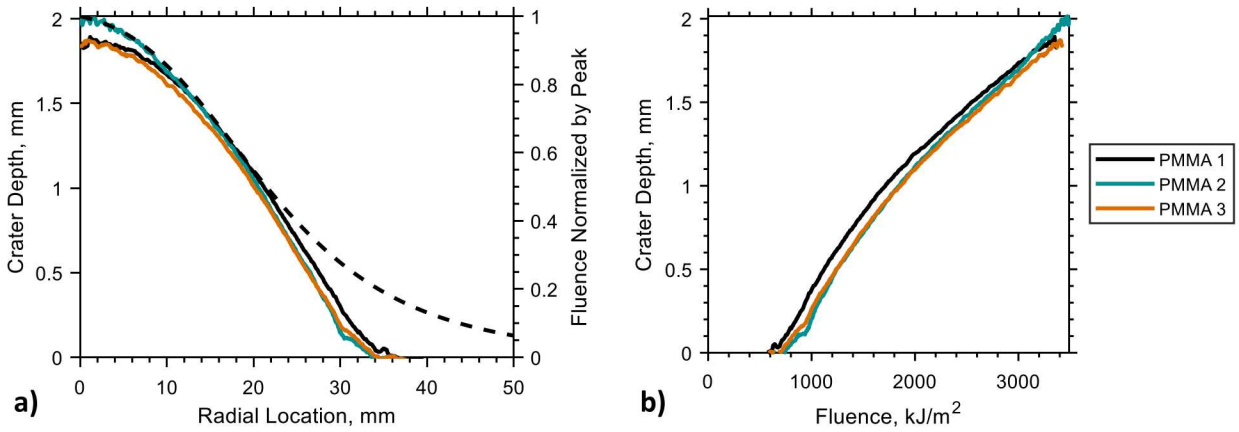

Fig. 5 Spatially resolved crater depth for PMMA samples. (a) The variation of crater depth with radial location is compared to the respective variation in fluence (dashed line). (b) The local fluence and crater depth are compared directly.

Table 2 Mass loss for PMMA samples. Data calculated from scanner are compared to those determined from pre- and post-test mass.

Sample	Exp. Fluence kJ m^{-2}	Act. Mass Loss (g)	Scan. Mass Loss (g)	Meas. Error (g)	Percent Error (%)
1	3780	2.70	3.07	0.37	13.5
2	3490	2.55	2.86	0.31	12.2
3	3430	2.55	2.79	0.24	9.4

2. Polystyrene

Overall, the response of the polystyrene samples was not as ideal as that of the PMMA samples. The crater depth was significantly smaller, affecting the strength of the signal and the accuracy of the results. The samples distorted from the exposure; the surface profiles varied by millimeters, as revealed by Fig. 6. The crater is not perceptible in the associated scan, in fact, the material is bulging outward by nearly 3 mm in the exposed region.

Extracting the crater depth from the front scan alone was not possible. A back side scan was used to account for the warping of the material. Figure 7b displays the front-surface profile after correcting for distortions using the back-surface scan. After this correction, nearly all evidence of warping is eliminated.

The crater is roughly 0.4 mm deep and has an approximate radius of 30 mm. The surface profile is higher around

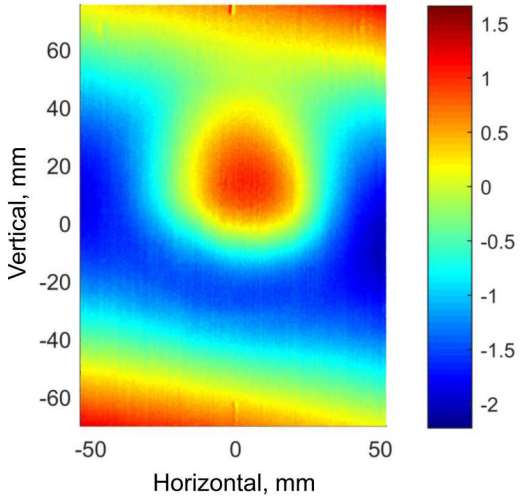

Fig. 6 Surface profile for a polystyrene sample determined by the front-surface scan. The material warped considerably, concealing the location and depth of the crater (the sample is bulging outward in the exposed region).

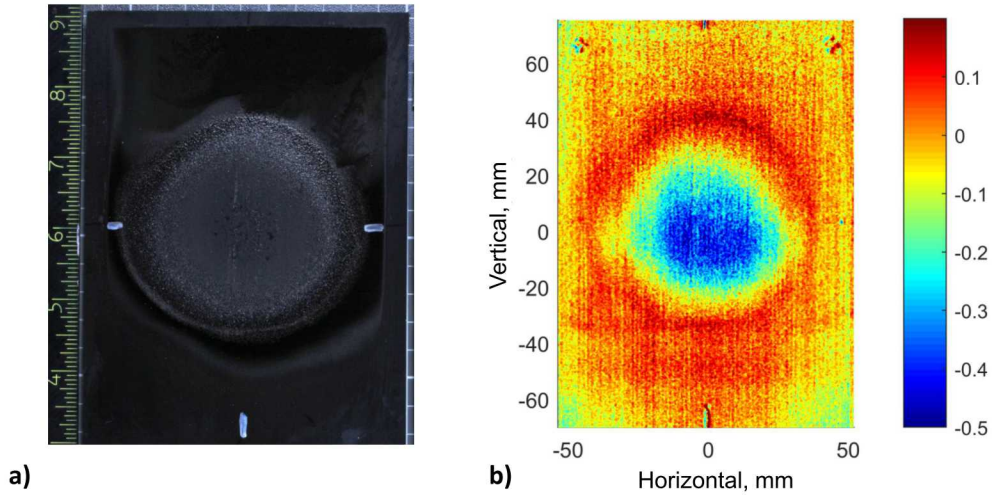

Fig. 7 Comparison of (a) Polystyrene-sample photograph and (b) the corresponding distortion-corrected surface profile. Ruler in photograph has units of inches. The surface profile (color bar) has units of millimeters.

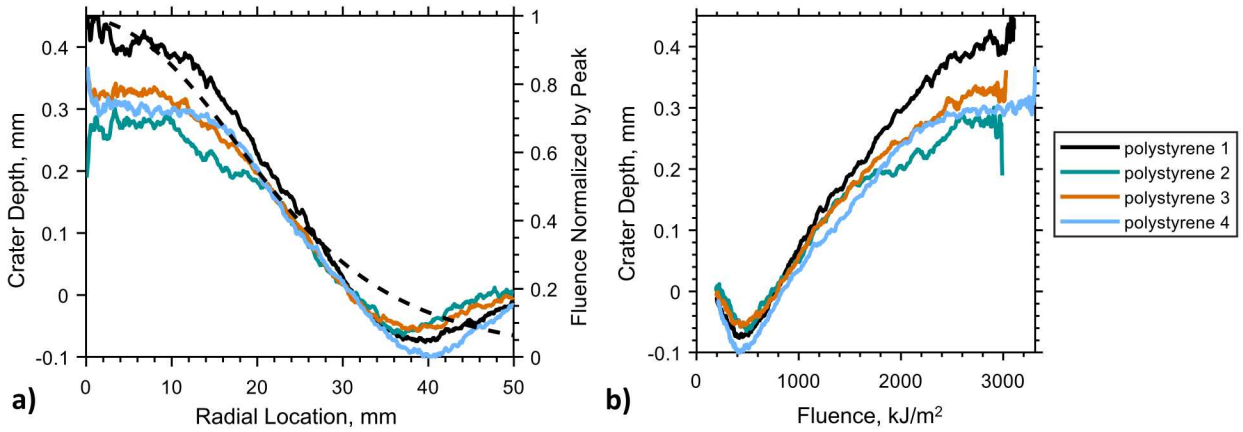

Fig. 8 Spatially resolved crater depth for polystyrene samples. (a) The variation of crater depth with radial location is compared to the respective variation in fluence (dashed line). (b) The local fluence and crater depth are compared directly.

Table 3 Mass loss for polystyrene samples. Data calculated from scanner are compared to those determined from pre- and post-test mass. The relatively large mass-loss errors may arise from swelling of the material during exposure.

Sample	Exp. Fluence kJ m^{-2}	Act. Mass Loss (g)	Scan. Mass Loss (g)	Meas. Error (g)	Percent Error (%)
1	3110	0.81	0.61	-0.20	-24.2
2	2990	0.78	0.42	-0.36	-46.6
3	3030	0.92	0.47	-0.45	-48.5
4	3320	0.89	0.50	-0.39	-44.0

the rim of the crater than the surrounding bulk material. The accompanying image, Fig. 7a, reveals surface roughness in the corresponding region. These features indicate the material may have expanded during the exposure.

The radial distribution for crater depth and exposure fluence is provided in Fig. 8. Variation between the samples is evident; in particular, the measured crater depth of sample 1 is much larger than the others. The crater depth also appears to plateau near the center of the crater ($r \approx 10$ mm). The onset of this plateau corresponds to a fluence of approximately 2500 kJ m^{-2}. The raised rim around the crater is clearly evident for radii between 30 mm and 50 mm.

The density of the virgin material was 1.06 g cm^{-3}. Equation 2 is applied to estimate the mass loss; the associated data and errors are provided in Table 3. The scanner data consistently underestimated the mass loss, possibly because the crater depth is comparable to the accuracy of the scanner. Alternatively, the material is swelling significantly throughout the crater, as around the rim in Fig. 7b. Swelling would effectively reduce the sample density and lower the predicted mass loss. Under these conditions, most of the inaccuracy indicated by Table 3 would be due to the assumptions of Equation 2; the surface topology would be correctly resolved (within the previously stated level of accuracy).

IV. Discussion

The three-dimensional scanner enhanced the analysis of the surface topology relative to traditional techniques (point measurements, cross sections, etc.). Using the spatially resolved surface height, the crater depth, swelling, and warping were quantified. These features were then correlated to the local exposure fluence, revealing interesting trends across the wide variety of materials tested. The results for polystyrene and PMMA are discussed below.

The variation of crater depth with fluence was relatively linear for the PMMA samples. These data indicate mass is vaporized in accordance with the local net energy delivered. Polystyrene did not exhibit this trend. The surface was raised (negative crater depth) at low fluence; meanwhile, crater depth begins to plateau at high fluence (Fig. 8). These trends indicate the physics governing thermal degradation of radiantly exposed polystyrene are more complex.

A nonlinear correlation between exposure fluence and crater depth could be caused by a few mechanisms. Charring or swelling of the material would affect the local surface topology by lowering the effective density of the material. While the scanner should still correctly identify the surface height in affected regions, the state of the sample in this region cannot be fully resolved. For example, the depth and density of a char layer cannot be determined; therefore, local mass loss and the sample chemistry are unknown. Sample cross sections are capable of providing better data of such features.

Charring or swelling of the polystyrene could justify the raised rim around the crater. Additionally, the char layers tend to suppress further material degradation, and consequently can explain the plateau in crater depth near the crater center. Radiation screening is another mechanism that could account for non-linear correlation of fluence to crater depth. Cameras deployed during the tests revealed that polystyrene produced an optically thick gas cloud relative to the PMMA samples. Optical screening by the pyrolyzate and the combustion products could cause the pyrolysis process to be self-terminating. Such behavior would affect regions with the highest flux, and thereby the most opaque boundary layer. The utility of the scanner for these and other qualitative trends is to identify physics that otherwise might be unrecognized and neglected.

Comparing the volume displacement to mass loss appeared to be a useful for PMMA samples. The mass-loss error was comparable to the surface-height error noted for the validation sample, namely: the error was positive and had a similar order of magnitude. The comparison of volume displacement and mass loss was less useful for the polystyrene samples. The mass loss was significantly underestimated by the scanner. These inaccuracies seem to be related to the charring and swelling effects discussed above.

The depth of the pyrolysis crater produced in the polystyrene samples was comparable to the accuracy of the 3D scanner. The relatively low magnitude of the surface height increased the relative uncertainty of the results and impeded discernment of surface features. Increasing the duration of the exposure would increase the strength of the measurement signal, improving the quality of the results. This approach would be particularly useful when the experiment is intended to reveal underlying physics or validate computational models, rather than replicate a specific thermal environment.

Particularly when multiple phenomena are interacting, the full surface topology of the exposed area is valuable for model validation activities. To fully describe the response of materials to the destructive environments, computational models must account for various phenomena, some of which are relevant to the surface profile. 3D reconstruction of the sample surface allows for direct comparison between the computational and the experimental results. These data can provide greater detail on the accuracy of physical models, such as those for pyrolysis, ablation, charring, and swelling.

The three-dimensional scanner provided useful data for many other materials not presented in this report. For example, some materials (e.g., wood) charred heavily from the exposure. The full surface topology allowed for quantitative description of this behavior. In some cases, such as the polystyrene samples examined in this report, the 3D scanner revealed surface profile variations that were otherwise not perceptible (e.g., 0.1 mm raised rim around the crater). In such cases, the 3D scans enhanced the presentation and interpretation of the data relative to qualitative descriptions based on visible features. Materials other than PMMA and polystyrene were excluded from this report because they did not conclusively demonstrate or contradict the utility of 3D scanners.

V. Conclusion

Scans on a validation sample indicated that the measurement accuracy of the instrument is roughly 0.1 mm, which is comparable to the advertised accuracy (0.13 mm). Depending on the nature of the sample, sample preparation (e.g., diffuse surface coatings) may be necessary to improve accuracy. The scanner accuracy seems to be dependent on the nature sample and the scanning technique; consequently, scanner validation should be repeated for external studies with different conditions, samples, and instruments.

Within the accuracy stated above, the scanner replicated the distortion of the bulk material, which could provide valuable data for many mechanical and thermal applications. For the present report, the distortion of the sample was neglected. Scans of the back surface of the sample corrected for distortion within the accuracy of the scanner. The distortion-corrected scans allowed for better imaging and analysis of the crater produced by the thermal environment.

This study indicates that commercial three-dimensional scanners can accurately resolve the topology of a damaged surface, but only examined a single scanner (NextEngine 3D Scanner Ultra HD) and samples with planar geometry and relatively smooth surface morphology. Spatially resolving the response of the surface (e.g., displacement, vaporization, ablation) enhanced the analysis of the corresponding experiments. The method is recommended for future studies, provided that the aforementioned accuracy is adequate and that the surface features span a sufficiently large area ($\sim$100 mm^2). Smaller features may be affected by the noise inherent to the measurement.

Acknowledgments

The authors thank Jeff LaRocco, Kevin Albrecht, and Scott Walkington for assisting with experimental operations at the Solar Furnace. Additionally, we thank Dan Worley, John Gray, and Noah Siegel for operating the 3D scanner and assisting with development of the technique. We also appreciate programmatic support from Jon Rogers (SNL). Funding was provided by the Defense Threat Reduction Agency. Sandia National Laboratories is a multimission laboratory managed and operated by National Technology and Engineering Solutions of Sandia, LLC, a wholly owned subsidiary of Honeywell International, Inc., for the U.S. Department of Energy's National Nuclear Security Administration under contract DE-NA0003525. This paper describes objective technical results and analysis. Any subjective views or opinions that might be expressed in the paper do not necessarily represent the views of the U.S. Department of Energy or the United States Government.

References

[1] Pineau, A., Benzerga, A. A., and Pardoen, T., "Failure of metals I: Brittle and ductile fracture," *Acta Materialia*, Vol. 107, 2016, pp. 424–483.

[2] Ndubizu, C. C., Ananth, R., and Tatem, P. A., "Transient burning rate of a noncharring plate under a forced flow boundary layer flame," *Combustion and Flame*, Vol. 141, No. 1-2, 2005, pp. 131–148.

[3] Rindal, R. A., Clark, K. J., and Flood, D. T., "Experimental and Theoretical Analysis of Ablative Material Response in a Liquid-Propellant Rocket Engine," Report, Aerotherm Corporation, 1967.

[4] Poon, C. Y., and Bhushan, B., "Comparison of surface roughness measurements by stylus profiler, AFM and non-contact optical profiler," *Wear*, Vol. 190, 1995, pp. 76–88.

[5] Grasselli, G., Wirth, J., and Egger, P., "Quantitative three-dimensional description of a rough surface and parameter evolution with shearing," *International Journal of Rock Mechanics & Mining Sciences*, Vol. 39, 2002, pp. 789–800.

[6] Ho, C., Khalsa, S., and Siegel, N., "Analytical methods to evaluate flux distributions from point-focus collectors for solar furnace and dish engine applications," *ASME 2010 4th International Conference on Energy Sustainability*, American Society of Mechanical Engineers, 2010, pp. 501–509.